

Low-Loss Space in Neural Networks is Continuous and Fully Connected

Yongding Tian^{1,*}, Zaid Al-Ars¹, Maksim Kitsak², Peter Hofstee^{1,3}

¹Computer Engineering Lab, Delft University of Technology

²Network Architectures and Services Group, Delft University of Technology

³IBM Infrastructure, Austin, TX

{Y.Tian-3,Z.Al-Ars,M.A.Kitsak,H.P.Hofstee}@tudelft.nl

Abstract

Visualizations of the loss landscape in neural networks suggest that minima are isolated points. However, both theoretical and empirical studies indicate that it is possible to connect two different minima with a path consisting of intermediate points that also have low loss. In this study, we propose a new algorithm which investigates low-loss paths in the full parameter space, not only between two minima. Our experiments on LeNet5, ResNet18, and Compact Convolutional Transformer architectures consistently demonstrate the existence of such continuous paths in the parameter space. These results suggest that the low-loss region is a fully connected and continuous space in the parameter space. Our findings provide theoretical insight into neural network over-parameterization, highlighting that parameters collectively define a high-dimensional low-loss space, implying parameter redundancy exists only within individual models and not throughout the entire low-loss space. Additionally, our work also provides new visualization methods and opportunities to improve model generalization by exploring the low-loss space that is closer to the origin.

1 Introduction

The training of neural networks is often understood as the process of optimizing a non-convex loss function to locate local or global minima [1]. Previous studies have visualized the loss function, referred to as the loss landscape, suggesting that minima are points, as demonstrated in Figure 1 of Foret et al. [2], Figure 1 and Figure 4 of Li et al. [3]. By using different random seeds, it is possible to find different minima, which suggests that the total low-loss space may be a collection of isolated points.

However, these loss landscape visualizations are limited to low-dimensional projections, far smaller than the full parameter space, typically represented as \mathbb{R}^D , where D denotes the number of trainable parameters. Recent theoretical advancements indicate that low-loss points should form connected regions rather than isolated points [4, 5, 6], implying the existence of a path where the loss remains consistently low. Empirical studies support this, demonstrating the feasibility of constructing paths between distinct low-loss points by slightly perturbing the linear interpolation between two low-loss points [7, 8].

In this study, we investigate the geometry of the low-loss space, defined as the set of all model parameters in \mathbb{R}^D that yield a loss below a specified threshold. Unlike previous studies which only constructs a low-loss path between two low-loss points [7, 8], our algorithms are able to find low-loss paths in the full \mathbb{R}^D space. We demonstrate that the low-loss space is not only continuous but also

*Corresponding author.

fully-connected as a single subspace within \mathbb{R}^D . By continuous, we mean that directions exist along which a low-loss model can be moved without leaving the low-loss space [9]. By fully-connected, we mean the entire low-loss space can be traversed without exiting this space.

The above statements are supported by our experimental results. We design two algorithms: (1) one algorithm to construct low-loss paths between two models and (2) one algorithm to construct low-loss paths from a low-loss point toward the origin. We test our algorithms on LeNet5 [10], ResNet18 [11], and Compact Convolutional Transformer (CCT7) [12]. Our results indicate that such paths consistently exist regardless of the low-loss points chosen, providing evidence that the low-loss space is both continuous and connected. Moreover, since these points represent models derived from independent training processes with different random seeds yet remain interconnected, we conclude that the low-loss space constitutes a fully-connected space. Compared to prior empirical work [8], our algorithms also yield paths with lower maximum loss, offering stronger quantitative support for the connectedness of the low-loss region.

Our further investigations of the low-loss space on selected models lead to three secondary observations. The first observation concerns parameter redundancy: we find that the low-loss space consistently has the same dimensionality as the full parameter space. This implies that all parameters actively contribute to defining the low-loss space. The common belief that neural networks are over-parameterized typically arises from analyses of individual low-loss models (low-loss points). While redundant parameters may exist at isolated points, the overall low-loss space itself exhibits no such redundancy.

The second observation involves visualization through principal component analysis (PCA). We apply PCA to project the low-loss space into two dimensions, offering a novel perspective on the representation of features captured by individual layers. The third observation focuses on the relationship between model generalization and weight variance—typically regulated through regularization techniques in existing studies [13, 14]. Our results suggest that it is possible to further improve the generalization of the state-of-the-art ResNet18 model, on top of existing data augmentation techniques [15] and training hyperparameters fine-tuning.

This paper makes several contributions to foundational neural network theory:

1. We define the low-loss space, a subspace in \mathbb{R}^D , as the collection of all models whose loss values are below a specified threshold. This low-loss space is deterministic, well-defined, and devoid of randomness. For any given model-dataset pair, the low-loss space is uniquely determined.
2. We introduce *Low-Loss Path Finding Algorithms*, which are capable of explicitly constructing paths among multiple low-loss points and toward the origin, enabling direct exploration of the geometry of the low-loss space. Empirical results on LeNet5, ResNet18, and CCT7 models indicate that the low-loss space is both continuous and connected as a single space.
3. We show that all parameters actively contribute to defining the low-loss space, thereby showing that neural network models in fact contains no redundant parameters on the low-loss space level. The redundancy in parameters is only valid when investigating single points in the low-loss space.
4. We apply principal component analysis (PCA) to project the low-loss space of LeNet5 into two dimensions. The resulting projection reveals potential representations of the features captured by each layer.
5. We visualize the relationship between model generalization and the variance of model weights. This approach provides a more direct and interpretable method than conventional techniques.

2 Related Work

Existing theoretical studies have shown that the low-loss region of neural network is continuous. Watanabe’s *Singular Learning Theory* (SLT) [16, 17, 18, 19], which is grounded in Bayesian learning, suggests that neural networks are singular models. The loss landscape of a singular model is a valley, with minima creating a continuous path at the bottom of the valley, as illustrated in Figure 3.1 of Carroll [5] and discussed in informal articles [20]. Additional studies reach similar conclusions by showing the existence of nearby low-loss points adjacent to a given minimum [4, 21].

Empirically, several algorithms have been proposed to construct continuous paths between two low-loss points. Among them, one of the most prominent is the Automated Nudged Elastic Band (AutoNEB) method [8]. AutoNEB begins by constructing a linear path between two models and then iteratively bends the path to reduce the loss at intermediate points. However, this method has several limitations. Most notably, it does not guarantee the discovery of a continuous low-loss path, as evidenced in Figure 3 of [8]². This limitation arises because the midpoint—typically the unweighted average of two models—often exhibits poor accuracy [22], thereby acting as a barrier along the path. In favorable scenarios, overcoming this barrier requires significant additional computational cost (as shown in Figure 5 of [8]); in less favorable cases, AutoNEB fails to find a viable path.

Other empirical efforts include studies that explore polynomial interpolation between low-loss points to approximate low-loss paths [7], as well as those that investigate the barriers on the interpolation [23, 24].

3 Low-Loss Path Finding Algorithm

This section describes the algorithm for finding low-loss paths in the parameter space \mathbb{R}^D . To ensure clarity and consistency with standard neural network terminology, we first introduce essential definitions and notations in Section 3.1, including the key concept of the *Variance Sphere*. Section 3.2 provides a detailed description of the Low-Loss Path Finding (LLPF) algorithm, and discusses its hyperparameters and prerequisites for its application.

3.1 Terminology and Definitions

To establish consistent terminology, we first revisit the procedure for training a neural network. The training process consists of the following steps:

1. Initialize model parameters $\theta_0 \in \mathbb{R}^D$ based on the model architecture \mathcal{M} .
2. Define a loss function \mathcal{L} and an optimization function \mathcal{O} , where \mathcal{O} includes all hyperparameters \mathbf{x} .
3. Prepare a dataset \mathcal{D} and divide it into batches, denoted as \mathcal{B} , satisfying $\mathcal{B} \subseteq \mathcal{D}$.
4. Given model parameters θ_t and a batch \mathcal{B}_t , compute the loss $L_t = \mathcal{L}(\theta_t, \mathcal{B}_t)$.
5. Update model parameters using $\theta_{t+1} = \mathcal{O}(\theta_t, \nabla L_t)$, where ∇L_t represents the gradient of L_t with respect to θ_t .

Steps 4 and 5 together constitute a single training iteration, denoted as $\text{Train}(\theta_t, \mathbf{x}, \mathcal{B}) \rightarrow \theta_{t+1}$, where \mathbf{x} encodes all training hyperparameters. For a well-designed model architecture \mathcal{M} and an appropriate choice of \mathcal{O} , the loss L_t is expected to converge to a local or global minimum after sufficient optimization iterations.

Since $\theta \in \mathbb{R}^D$, the parameters θ can be interpreted as a point P in the high-dimensional parameter space \mathbb{R}^D . Each point P is also associated with a loss value L , which could be calculated with $L = \mathcal{L}(P, \mathcal{D})$. We define the low-loss space to be the collection of all points P that result in a loss that is smaller than a threshold value L_{thres} . The low-loss space, denoted as $S_{L \leq L_{\text{thres}}}$, is defined in Equation 1.

$$S_{L \leq L_{\text{thres}}} := \{P \in \mathbb{R}^D \mid \mathcal{L}(P, \mathcal{D}) \leq L_{\text{thres}}\} \quad \text{definition of \textbf{Low-Loss Space}} \quad (1)$$

Unlike local minima, which are discovered through stochastic processes, the low-loss space is a well-defined region for a given model architecture \mathcal{M} and dataset \mathcal{D} , denoted as $\text{LLS}(\mathcal{M}, \mathcal{D}) = S_{L \leq L_{\text{thres}}}$. While it is theoretically possible to identify this space by evaluating the loss across \mathbb{R}^D , such exhaustive search is infeasible due to the high dimensionality of modern neural networks.

Because neural networks are structured in layers, the set of parameters θ can be decomposed as $[\theta_{l_0}, \dots, \theta_{l_x}, \dots, \theta_{l_n}]$, where l_x represents the layers defined in \mathcal{M} . Each layer's parameters are represented as $\theta_{l_x} \in \mathbb{R}^{d_{l_x}}$, where d_{l_x} denotes the number of trainable parameters for layer l_x .

²In contrast, our algorithm demonstrates significantly more consistent low-loss paths.

Since the layer parameters can be viewed as a distribution of real numbers, we define the variance of this distribution as $\text{Var}(\theta_{l_x})$. We then define a region in $\mathbb{R}^{d_{l_x}}$ consisting of all points θ_{l_x} that satisfy the condition $\text{Var}(\theta_{l_x}) = v$. This region, referred to as the **Variance Sphere** (S_{var}), forms a high-dimensional sphere in $\mathbb{R}^{d_{l_x}}$. For consistency, we use the point notation P_{l_x} instead of θ_{l_x} in the formal definition of the Variance Sphere, given in Equation 2.

$$S_{\text{var}=v} := \{P_{l_x} \in \mathbb{R}^{d_{l_x}} \mid \text{Var}(P_{l_x}) = v\} \quad \text{definition of \textbf{Variance Sphere}} \quad (2)$$

In typical model training procedures, the parameters of linear layers, convolutional layers, and transformer layers are initialized as a distribution with a specific variance and mean. The mean is usually set to zero, while the variance is determined by one of the following methods: LeCun [25], Xavier [26], or Kaiming [27]. The number of trainable parameters also affects initialization, as all above methods compute variance based on the number of trainable parameters in the given layer. This relationship is mathematically expressed in Equation 3.

$$\theta_0, \theta'_0 = \text{Init}(\mathcal{M}) \implies \text{Var}(\theta_0) = \text{Var}(\theta'_0) \quad (3)$$

Our experimental results indicate that models trained with identical hyperparameters tend to be positioned on variance spheres that are close to each other. However, this observation is not universally applicable across all model architectures and must be empirically validated before applying our algorithms. Our experimental validation of this relationship for ResNet18 is provided in Appendix A.1. This relationship is mathematically expressed in Equation 4.

$$\theta_n = \text{Train}^n(\theta_0, \mathbf{x}, \mathcal{D}), \quad \theta'_n = \text{Train}^n(\theta'_0, \mathbf{x}, \mathcal{D}) \implies \text{Var}(\theta_n) \approx \text{Var}(\theta'_n) \quad (4)$$

Train denotes a training iteration, where \mathbf{x} represents all training hyperparameters, including learning rate, momentum, and weight decay, etc. The symbol \mathcal{D} refers to the training dataset. The operator Var calculates the variance of model parameters θ . Since a model consists of multiple layers, the result of the Var operator is a vector. For single-layer parameters θ_{l_x} , the Var operator returns a scalar value.

In this paper, we make one approximation: the center of the variance spheres $S_{\text{var}=v}$ is close to the origin, expressed as:

$$\text{Mean}(\theta_{l_x}) \approx 0 \quad (5)$$

This equation holds due to the following reasons: (1) during initialization, layer weights (excluding normalization layers) are set to a distribution with zero mean; (2) after training iterations, the mean of layer weights deviates from zero. This deviation is small and can be ignored since it does not influence our algorithms. We justify this approximation empirically in Appendix A.2.

From Equation 5, we derive that the variance of the coordinates of a point P (where $P \in S_{\text{var}=v}$) is approximately proportional to the squared Euclidean distance from P to the origin O in $\mathbb{R}^{d_{l_x}}$, expressed as:

$$\|\overrightarrow{OP_{l_x}}\|^2 \propto \text{Var}(\theta_{l_x}) \quad (\text{approximately}) \quad (6)$$

The full derivation is provided in Appendix A.3.

3.2 LLPF Algorithm

We propose the *Low-Loss Path Finding* (LLPF) algorithm to explore the subspace $\mathcal{S}_{L < L_{\text{thres}}} \subset \mathbb{R}^D$, which comprises all model parameters yielding a loss below a specified threshold. LLPF is composed of two complementary components. The first, referred to as the *model-to-model* algorithm (LLPF_M2M), constructs a path between two low-loss models located on variance spheres with a small variance difference—that is, satisfying the condition in Equation 4. This procedure is detailed in Algorithm 1. The second component, the *model-to-origin* algorithm (LLPF_M2O), generates a path from a low-loss model toward the origin of \mathbb{R}^D , as described in Algorithm 2. These components serve distinct purposes: Algorithm 1 enables exploration within the same variance sphere, while Algorithm 2 enables exploration across variance spheres.

The geometric intuition behind Algorithm 1 is illustrated in Figure 1, using the notation of the algorithm, including points P_0, P_1, M_1, M_2 , and M_3 . The algorithm starts by moving the starting P_0 slightly toward the destination D to obtain M_1 via a weighted average(Move, Line 5), controlled

by hyperparameters $step_f$ and $step_a$. Next, the *VarianceCorrection* step projects M_1 back as M_2 onto the variance sphere of P_0 to counteract the vanishing variance problem, a phenomenon wherein averaging uncorrelated neural networks leads to reduced parameter variance, thereby hindering subsequent training efforts (see [28]). M_2 is refined through r training steps to reduce loss below threshold, yielding M_3 , which is again projected back to the sphere to produce P_1 , which serves as the new starting point for the next iteration. Repeating this process for T iterations yields a continuous low-loss path $\{P_i\}$ from P_0 to $P_T \approx D$.

The mechanism of Algorithm 2 is similar to that of Algorithm 1, with two key differences: the removal of the *VarianceCorrection* step and the inclusion of an *AngleConformal* step. The *AngleConformal* step is introduced to adaptively reduce the learning rate as the variance decreases. This adjustment is necessary because applying the learning rate appropriate for a large variance sphere³ to a small variance sphere often causes the model to deviate from the low-loss path. Although Algorithm 2 can theoretically be applied in reverse (to move a model toward a larger variance sphere) we observe that this process frequently suffers from exploding gradients problem [29]. Consequently, the reverse direction is omitted.

Hyperparameters

The hyperparameters used in this paper for Algorithm 1 and Algorithm 2 are listed in Appendix A.6. In addition to traditional hyperparameters such as learning rate and optimizer, there are several algorithm-specific hyperparameters and design principles to consider, which we discuss below.

For both algorithms, two hyperparameters directly influence the quality of the low-loss paths. The first is $step_a$ and $step_f$, which control the continuity of the path—smaller values lead to smaller distances between consecutive points P_i and P_{i+1} . The second is r , which determines how low the training loss can go—larger values correspond to more training iterations and potentially lower loss. However, higher-quality paths come at the cost of increased computational workload, so the computation budget must be considered.

The most critical hyperparameters for successfully finding a low-loss path using Algorithm 1 are the selection and order of layers to which the algorithm is applied. This is because Algorithm 1 operates on a single layer at a time, as the variance sphere is defined at the layer level (denoted as d_{l_x} in Equation 2). For simple low-loss spaces, such as LSS(LeNet5, MNIST), the algorithm can be applied to all layers simultaneously. However, this strategy fails in more complex settings, such as LSS(ResNet18, CIFAR10), where the loss barrier at the midpoint still exists,

Algorithm 1 LLPF_M2M: Algorithm for constructing a low-loss path between two models. The major steps of this algorithm are also illustrated in the geometry plot in Figure 1, which uses consistent point notations as this algorithm.

```

function LLPF_M2M( $P_0, D$ )           ▷  $P_0$ : starting point,  $D$ :
destination point
2:    $P_0, D \in \text{Flat Low Loss Region}$ 
    $P_i = P_0$ 
4:   for  $i = 0$  to  $T$  do
        $M_1 = \text{Move}(P_i, D, step_f, step_a)$  ▷ Corresponding to
        $\overrightarrow{P_0 M_1}$ 
6:    $M_2 = \text{VarianceCorrection}(M_1, S_{var})$  ▷ Corresponding
       to  $\overrightarrow{M_1 M_2}$ 
        $M_3 = \text{Train}^r(M_2, \mathbf{x}, \mathcal{B})$  ▷ Corresponding to  $\overrightarrow{M_2 M_3}$ .
       Training  $r$  steps with hyper-parameters  $\mathbf{x}$ 
8:    $P_{i+1} = \text{VarianceCorrection}(M_3, S_{var})$  ▷
       Corresponding to  $\overrightarrow{M_3 P_1}$ 
   end for
10:  return  $P_0 \dots P_n$            ▷ Final output of LLPF_M2M
end function

12:  function MOVE( $P_i, D, step_f, step_a$ )
14:     $step = step_a |\overrightarrow{P_i D}| + step_f$ 
        $M_1 = P_i + step \overrightarrow{P_i D}$ 
16:    return  $M_1$ 
end function

18:  function VARIANCECORRECTION( $W, S_{var=v}$ ) ▷  $W$  is treated
as an array
20:     $\bar{W} = \frac{1}{n} \sum_{i=1}^n W[i]$  ▷ Compute mean of  $W$ ,  $i$  indicates the
element index
        $\sigma_W^2 = \frac{1}{n} \sum_{i=1}^n (W[i] - \bar{W})^2$  ▷ Compute variance of  $W$ 
22:    for  $i$  in  $\text{len}(W)$  do           ▷  $i$  indicates the element index
        $W'[i] = \bar{W} + \sqrt{\frac{v}{\sigma_W^2}} (W[i] - \bar{W})$  ▷ Scale variance
24:    end for
       return  $W'$ 
26: end function

```

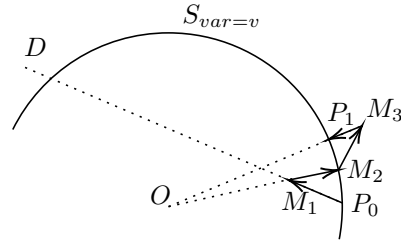


Figure 1: Geometric illustration of the first iteration of Algorithm 1, showing the transition from P_0 to P_1 . Point labels follow the algorithm’s notation. The origin is used as the center of the variance sphere, assuming the mean is approximately zero (Equation 5 and Equation 6).

³A large variance sphere refers to a variance sphere with a high variance value.

as discussed in Section 2. In such cases, a layer-by-layer application in a carefully determined order is necessary. An illustration of this process for ResNet18 and CCT7 is provided in Appendix A.6 Table 1.

For Algorithm 1, the optimizer should exclude regularization techniques such as weight decay, as the constraint of remaining within a single variance sphere already ensures that the variance of the layer weights is preserved. Additionally, momentum is generally avoided in this setting. While momentum is usually used to stabilize long-distance training trajectories, it is less suitable here, as the update steps in Algorithm 1 are small and localized.

Algorithm 2 shares similar hyperparameters with Algorithm 1, but with two key differences: (1) the selection and order of layers is less critical, as moving all layers simultaneously successfully finds a low-loss path in our experiments; (2) normalization layers should be excluded from the Algorithm 2, since their purpose is to rescale outputs to zero mean and unit variance, and moving them toward the origin reduces their weight variance, thereby impairing their functionality.

Prerequisite

Algorithm 1 has two prerequisites. First, corresponding layers of the input models must lie on nearby variance spheres, as defined in Equation 4; a counterexample is VGG16 (without batch normalization) on CIFAR-10, where both Algorithm 1 and Algorithm 2 are needed to explore the low-loss space. Second, shared with Algorithm 2, input models should lie in flat low-loss regions, similar to the structure shown in Figure 1 (right) of [2]. Empirically, we find that starting from sharp minima can cause our algorithm fail to find feasible paths. This is likely because sharp minima are surrounded by many local minima, increasing the chance of our algorithm getting trapped. In our experiments, ResNet18 models trained with the Adam optimizer on CIFAR-10 tend to converge to sharp minima, preventing Algorithm 1 from constructing a valid low-loss path⁴. While sharpness is hard to measure precisely, we find that minima with near-zero training loss are generally flat and suitable as starting points.

Algorithm 2 The algorithm to find the low-loss path across different S_{var} .

```

function LLPF_M2O( $P_0$ )                                ▷  $P_0$ : starting point
2:    $P_0 \in \text{Flat Low Loss Region}$ 
    $P_i = P_0$ 
4:    $P_0 \in S_{var=v}$                                        ▷ Variance of  $P_0$  is  $v$ 
   for  $i = 0$  to  $n$  do
6:      $N = \text{Move}(P_i, O, \text{step}_f, \text{step}_a)$                ▷ Move toward
origin  $O$ 
      $\mathbf{x} = \text{AngleConformal}(N, v)$                        ▷ Adjust training
hyper-parameters based on  $N$ 's variance
8:      $P_{i+1} = \text{Train}^r(N, \mathbf{x}, \mathcal{B})$                  ▷ Training  $r$  steps with
hyper-parameters  $\mathbf{x}$ 
     end for
10: end function

12: function ANGLECONFORMAL( $N, v$ )
    $N \in S_{var=w}$                                           ▷ calculate the variance of  $N$  to be  $w$ 
14:    $\eta = \frac{\eta_{base} \cdot w}{v}$                                ▷ Scale learning rate  $\eta$  to maintain angular
conformity
    $\mathbf{x} = \eta, \dots$                                        ▷ Include all other hyper-parameters
16:   return  $\mathbf{x}$ 
end function

```

4 Experimental Evaluation of Low-Loss Path Finding Algorithms

This section presents the results of applying Algorithm 1 and Algorithm 2 to explore the LLS(LeNet5, MNIST [30]), LLS(ResNet18, CIFAR10 [31]) and LLS(CCT7, CIFAR10), as shown in Figure 2 and Figure 3. To ensure consistency of the results, we repeat each experiment 200, 40, and 10 times, respectively, using different low-loss models trained with identical hyperparameters. Full hyperparameter settings are listed in Appendix A.6.

In Figure 2, we assess path validity using three criteria: (1) the training loss must remain below L_{thres} (first row); (2) the distance between P_i and D should gradually converge to zero (second row), with minor deviations allowed due to Equation 4, which states that the starting point P_0 and destination D lie approximately—but not exactly—on the same variance sphere; and (3) the final testing loss should converge to the testing loss at iteration 0, since the final point is expected to converge to D , which should exhibit similar generalization behavior as P_0 . In our results, all training losses remain below 0.1, and the final layer-wise distances gradually converges below 10^{-1} , indicating that the low-loss paths in Figure 2 are correctly constructed.

The third row of Figure 2 shows test accuracy and loss along the paths. However, we observe that Algorithm 1 does not guarantee low testing loss, as seen in the ResNet18 case, where test loss increases despite low training loss. This is because the algorithm operates within the training-defined low-loss space (Equation 1), which is not align with the testing dataset.

⁴This issue can be addressed using the configuration in Table 3.

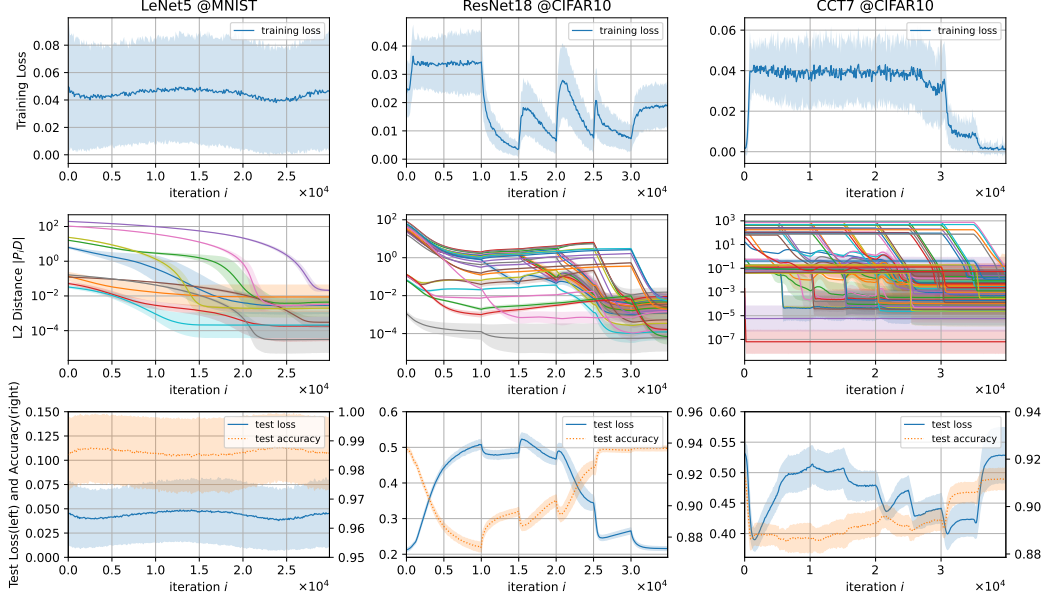


Figure 2: Results of Algorithm 1. Each column corresponds to a different model and dataset: LeNet5@MNIST (first column), ResNet18@CIFAR10 (second column), and CCT7@CIFAR10 (third column). The first row shows the training loss; the second row shows the layer-wise L2 distance between P_i and the destination point D ; and the third row shows the test loss and test accuracy of the whole testing dataset. Legends for the second row are omitted due to the large number of layers. Each experiment is repeated with different starting and destination models, trained from different random seeds. The curves show the mean across repetitions, and the shaded regions indicate the standard deviation. Both the curves and the shaded boundaries are smoothed using a moving average with a window size of 10.

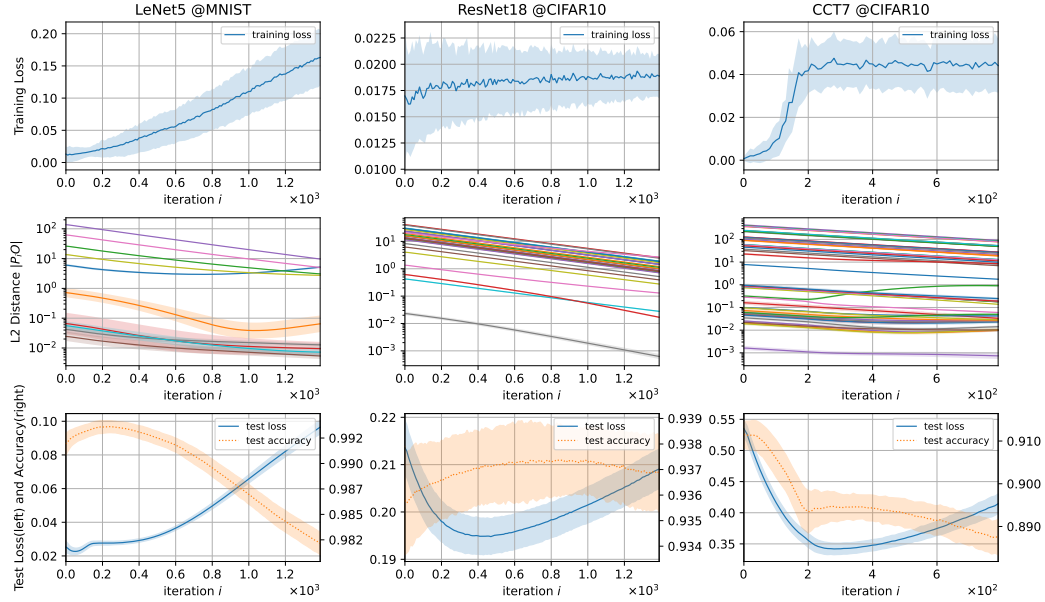


Figure 3: Results of Algorithm 2, following the same layout and postprocessing steps as in Figure 2, except that all normalization layers are excluded from the second row, as Algorithm 2 does not operate on them. Since the origin is not a low-loss model, the training loss is not expected to remain low, nor is the layer-wise L2 distance expected to reach zero. For LeNet5 and ResNet18, we reduce the layer variance by a factor of 0.76, and for CCT7, layer variance is reduced by a factor of 0.55. Thus, our setting explores more than 50% of the path toward the origin.

Figure 3 highlights additional insights. First, LeNet5 shows increasing training loss as all layers move toward the origin and their variances decrease. In contrast, ResNet18 avoids this issue as its normalization layers are excluded from movement. Second, we observe a peak in test accuracy or a minimum in test loss along the path toward the origin. This phenomenon aligns with the intuition behind model regularization techniques, such as L2 norm and weight decay, which encourage models to stay closer to the origin to improve model generalization [32, 33]. Unlike traditional methods requiring hyperparameter tuning, Algorithm 2 reveals a smoother post-training relationship between generalization and distance to the origin, offering a more efficient alternative.

Comparing LLPF with AutoNEB

We also compare LLPF with AutoNEB [8], which bends linear interpolation between low-loss models to form a low-loss path. Our proposed LLPF algorithms differ from AutoNEB in several key aspects. First, unlike AutoNEB, which often finds paths with low testing loss, LLPF does not guarantee this, highlighting an inherent difference in the resulting low-loss paths. Second, LLPF-generated paths exhibit consistent properties, such as test loss and L2 distance to the origin, across different simulations, as shown by the narrow shaded regions in Figure 2 and Figure 3, whereas AutoNEB paths are often inconsistent, as shown in Figure 7 of [8]. Third, AutoNEB does not explore regions near the origin, while Algorithm 2 explicitly targets this space. Fourth, our algorithm can be configured to explore low-loss spaces with even lower loss than those found by AutoNEB. This result is presented in Appendix A.7.

The result in Appendix A.7 also provides quantitative support for the continuity of the low-loss space. Since models can have much smaller loss values than low-loss paths, our ability to construct a path with a maximum loss lower than AutoNEB’s minimum loss offers stronger empirical evidence that continuous low-loss paths exist between low-loss models.

5 Geometric and Generalization Properties of the Low-Loss Space

In this section, we present additional explorations of the low-loss space. First, we argue that a low-loss space is continuous and fully connected, as the LLPF algorithms consistently construct low-loss paths with stable properties. Second, we use principal component analysis to project low-loss paths into two dimensions for visualization. Third, we examine the number of low-loss paths starting from a given trained model and find that they span a space with the same dimensionality as the full parameter space, indicating the low-loss space has no redundant parameters. Finally, we apply Algorithm 2 to CIFAR10 and ImageNet1k to evaluate its effect on model generalization.

The low-loss space is continuous and fully connected

As shown in Figure 2, the results are consistent across repetitions—200 for LeNet5, 40 for ResNet18, and 10 for CCT7—with each model trained using identical hyperparameters but different random seeds. This supports the claim that, for any two low-loss models trained under the same setup, LLPF can reliably construct a continuous path, implying that the low-loss space is fully connected within a single variance sphere. Connectivity across different variance spheres is demonstrated using Algorithm 2 (Figure 3). While our results indicate that low-loss regions are also connected across variance spheres, a boundary exists, as the origin itself is not a low-loss point.

PCA visualization of the low-loss space

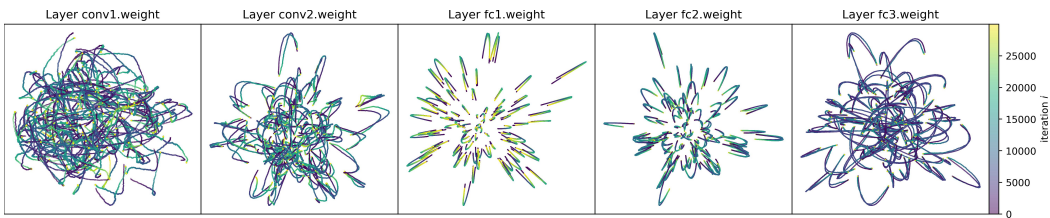


Figure 4: Principal Component Analysis(PCA) visualization of LLS(LeNet5, MNIST). Each panel shows the 2D PCA projection of one layer. This figure is obtained by generating two sets of 100 low-loss models, denoted $[A_0 \dots A_{99}]$ and $[B_0 \dots B_{99}]$. For each pair (A_i, B_i) , we construct low-loss paths from A_i to B_i and vice versa. The resulting high-dimensional paths are recorded and projected into 2D using PCA. The color indicates the iteration index i in Algorithm 1.

We visualize the low-loss paths of LLS(LeNet5, MNIST) using Principal Component Analysis (PCA) to project high-dimensional paths into two dimensions (Figure 4). Notably, the first layer (`conv1.weight`) exhibits more high-frequency changes than other layers. These changes suggest sharper regions in the loss landscape [2]. Since each point in Figure 4 represents a low-loss model (i.e., a local minimum on the loss landscape), a flatter landscape leads to smoother paths, while a sharper landscape results in more abrupt changes along the path.

We attribute the concentration of high-frequency changes in the first layer to its sensitivity to the input-level high-frequency features. This effect is less pronounced in ResNet18 (Appendix A.5, Figure 9), likely due to residual connections that propagate high-frequency information to deeper layers. This supports the argument that residual connections contribute to flatter loss landscapes and improved generalization [3] by mitigating feature congestion in early layers. Therefore, PCA visualizations of the low-loss space has the potential to serve as a layer-wise diagnostic tool to analyze the types of features captured by each layer.

Low loss space has no redundant parameters

Figure 4 raises an important question: what is the dimensionality of the low-loss space? Given the symmetric nature of the parameter space [34], no parameter is inherently special. This suggests that all parameters contribute to the low-loss space, and the low-loss space should have the same dimensionality as the parameter space. We empirically verify this intuition through the following analysis.

The low-loss space for a single layer lies on a variance sphere in $\mathbb{R}^{d_{l_x}}$, providing an upper bound on its dimensionality. To estimate a lower bound, we construct multiple low-loss paths from the same trained model—each generated via a single training iteration with large batch size and multiple steps to ensure movement follows true low-loss directions. Applying Singular Value Decomposition (SVD) to the set of resulting parameter vectors, we find that the dimensionality of the spanned subspace consistently equals either the minimum of the number of paths or the parameter dimensionality. This confirms that the low-loss space spans the full parameter space, indicating that no parameter is redundant in defining it.

Better model generalization on smaller variance spheres

Based on the observation in Figure 3 that models on smaller variance spheres tend to generalize better, we further validate this for ResNet18 on CIFAR100 and ImageNet1k [35]. The results are shown in Figure 5. The most notable finding is from ImageNet1k: using the pretrained start-of-the-art ResNet18 weights from PyTorch [36]—which already achieve 69.758% test accuracy with fine-tuned hyperparameters—Algorithm 2 improves generalization further, reaching 70.55% test accuracy—without additional data augmentation. This suggests that current hyperparameter search methods may be incomplete. In particular, optimal hyperparameters might be layer-specific, since normalization layers are not moved toward the origin in Algorithm 2. As layer-wise hyperparameter tuning is often computationally intensive, exploiting the fully connected structure of the low-loss space may offer a more efficient alternative for improving generalization.

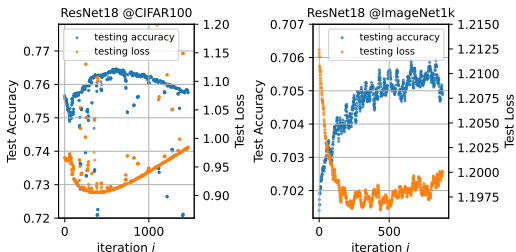


Figure 5: Results of applying Algorithm 2 on CIFAR100 and ImageNet1k. For CIFAR100, a low-loss model is trained using the hyperparameters in Table 3, while for ImageNet1k, we use the pretrained state-of-the-art model from PyTorch. In both cases, Algorithm 2 further improves model generalization.

6 Conclusion

This paper presents a set of novel low-loss path finding algorithms, which construct low-loss paths in the full parameter space. Empirical evaluations on LeNet5@MNIST, ResNet18@CIFAR10, and CCT7@CIFAR10 show that the corresponding low-loss spaces are continuous and fully connected. Our investigation of these low-loss spaces yields several key findings. First, all parameters actively contribute to defining the low-loss space, indicating no parameter is redundant at the low-loss space

level. Second, PCA-based visualization of the low-loss space provides layer-wise insights into the features captured by each layer. Third, the full connectivity of the low-loss space suggests a potential alternative to hyperparameter fine-tuning: leveraging connectivity to traverse the space more efficiently for improved generalization, without modifying regularization settings.

Acknowledgments and Disclosure of Funding

This work used the Dutch national e-infrastructure with the support of the SURF Cooperative using grant no. EINF-5527 and no. EINF-9661. In addition, this work was performed with the support of the Eureka Xecs project TASTI (grant no. 2022005).

References

- [1] Quynh Nguyen and Matthias Hein. The loss surface of deep and wide neural networks. In *Proceedings of the 34th International Conference on Machine Learning - Volume 70, ICML'17*, page 2603–2612, 2017.
- [2] Pierre Foret, Ariel Kleiner, Hossein Mobahi, and Behnam Neyshabur. Sharpness-aware minimization for efficiently improving generalization. In *International Conference on Learning Representations*, 2021.
- [3] Hao Li, Zheng Xu, Gavin Taylor, Christoph Studer, and Tom Goldstein. Visualizing the loss landscape of neural nets. In Samy Bengio, Hanna M. Wallach, Hugo Larochelle, Kristen Grauman, Nicolò Cesa-Bianchi, and Roman Garnett, editors, *Advances in Neural Information Processing Systems 31: Annual Conference on Neural Information Processing Systems 2018, NeurIPS 2018, December 3-8, 2018, Montréal, Canada*, pages 6391–6401, 2018.
- [4] Henning Petzka and Cristian Sminchisescu. Non-attracting regions of local minima in deep and wide neural networks. *J. Mach. Learn. Res.*, 22(1), January 2021.
- [5] Liam Carroll. Phase transitions in neural networks. Master’s thesis, The University of Melbourne, October 2021.
- [6] C. Daniel Freeman and Joan Bruna. Topology and geometry of half-rectified network optimization, 2017.
- [7] Timur Garipov, Pavel Izmailov, Dmitrii Podoprikin, Dmitry P Vetrov, and Andrew G Wilson. Loss surfaces, mode connectivity, and fast ensembling of dnns. In S. Bengio, H. Wallach, H. Larochelle, K. Grauman, N. Cesa-Bianchi, and R. Garnett, editors, *Advances in Neural Information Processing Systems*, volume 31. Curran Associates, Inc., 2018.
- [8] Felix Draxler, Kambis Veschgini, Manfred Salmhofer, and Fred Hamprecht. Essentially no barriers in neural network energy landscape. In Jennifer Dy and Andreas Krause, editors, *Proceedings of the 35th International Conference on Machine Learning*, volume 80 of *Proceedings of Machine Learning Research*, pages 1309–1318. PMLR, 10–15 Jul 2018.
- [9] G. E. Bredon. Topology and geometry. *Graduate Texts in Mathematics*, 1993.
- [10] Y. Lecun, L. Bottou, Y. Bengio, and P. Haffner. Gradient-based learning applied to document recognition. *Proceedings of the IEEE*, 86(11):2278–2324, 1998.
- [11] Kaiming He, Xiangyu Zhang, Shaoqing Ren, and Jian Sun. Deep residual learning for image recognition, 2015.
- [12] Ali Hassani, Steven Walton, Nikhil Shah, Abulikemu Abuduweili, Jiachen Li, and Humphrey Shi. Escaping the big data paradigm with compact transformers, 2022.
- [13] Guodong Zhang, Chaoqi Wang, Bowen Xu, and Roger Grosse. Three mechanisms of weight decay regularization. In *International Conference on Learning Representations*, 2019.
- [14] Ilya Loshchilov and Frank Hutter. Decoupled weight decay regularization. In *International Conference on Learning Representations*, 2019.
- [15] Alhassan Mumuni and Fuseini Mumuni. Data augmentation: A comprehensive survey of modern approaches. *Array*, 16:100258, 2022.
- [16] Sumio Watanabe. Almost all learning machines are singular. In *2007 IEEE Symposium on Foundations of Computational Intelligence*, pages 383–388, 2007.
- [17] Sumio Watanabe. *Algebraic Geometry and Statistical Learning Theory*. Cambridge Monographs on Applied and Computational Mathematics. 2009.
- [18] Sumio Watanabe. A widely applicable bayesian information criterion. *J. Mach. Learn. Res.*, 14(1):867–897, March 2013.

- [19] Sumio Watanabe. *Mathematical Theory of Bayesian Statistics*. CRC Press, Taylor & Francis Group, Boca Raton, 2018.
- [20] Neural networks generalize because of this one weird trick — LessWrong — lesswrong.com. <https://www.lesswrong.com/posts/fovfuFdpuEwQzJu2w/neural-networks-generalize-because-of-this-one-weird-trick>. [Accessed 07-04-2025].
- [21] T. Poston, C.-N. Lee, Y. Choie, and Y. Kwon. Local minima and back propagation. In *IJCNN-91-Seattle International Joint Conference on Neural Networks*, volume ii, pages 173–176 vol.2, 1991.
- [22] Cheng Ju, Aurélien Bibaut, and Mark J. van der Laan. The relative performance of ensemble methods with deep convolutional neural networks for image classification, 2017.
- [23] Tiffany Vlaar and Jonathan Frankle. What can linear interpolation of neural network loss landscapes tell us?, 2022.
- [24] Ian J. Goodfellow, Oriol Vinyals, and Andrew M. Saxe. Qualitatively characterizing neural network optimization problems, 2015.
- [25] Yann LeCun, Léon Bottou, Genevieve B. Orr, and Klaus-Robert Müller. Efficient backprop. In *Neural Networks: Tricks of the Trade, This Book is an Outgrowth of a 1996 NIPS Workshop*, page 9–50, Berlin, Heidelberg, 1998. Springer-Verlag.
- [26] Xavier Glorot and Yoshua Bengio. Understanding the difficulty of training deep feedforward neural networks. In Yee Whye Teh and Mike Titterton, editors, *Proceedings of the Thirteenth International Conference on Artificial Intelligence and Statistics*, volume 9 of *Proceedings of Machine Learning Research*, pages 249–256, Chia Laguna Resort, Sardinia, Italy, 13–15 May 2010. PMLR.
- [27] Kaiming He, Xiangyu Zhang, Shaoqing Ren, and Jian Sun. Delving deep into rectifiers: Surpassing human-level performance on imagenet classification. In *2015 IEEE International Conference on Computer Vision (ICCV)*, pages 1026–1034, 2015.
- [28] Yongding Tian, Zaid Al-Ars, Maksim Kitsak, and Peter Hofstee. Vanishing variance problem in fully decentralized neural-network systems, 2024.
- [29] Boris Hanin. Which neural net architectures give rise to exploding and vanishing gradients? In *Proceedings of the 32nd International Conference on Neural Information Processing Systems, NIPS’18*, page 580–589, Red Hook, NY, USA, 2018. Curran Associates Inc.
- [30] Li Deng. The mnist database of handwritten digit images for machine learning research [best of the web]. *IEEE Signal Processing Magazine*, 29(6):141–142, 2012.
- [31] Alex Krizhevsky. Learning multiple layers of features from tiny images. *University of Toronto*, 05 2012.
- [32] Aitor Lewkowycz and Guy Gur-Ari. On the training dynamics of deep networks with l2 regularization. In *Proceedings of the 34th International Conference on Neural Information Processing Systems, NIPS ’20*, Red Hook, NY, USA, 2020. Curran Associates Inc.
- [33] Anders Krogh and John Hertz. A simple weight decay can improve generalization. In J. Moody, S. Hanson, and R.P. Lippmann, editors, *Advances in Neural Information Processing Systems*, volume 4. Morgan-Kaufmann, 1991.
- [34] Derek Lim, Theo Moe Putterman, Robin Walters, Haggai Maron, and Stefanie Jegelka. The empirical impact of neural parameter symmetries, or lack thereof, 2024.
- [35] Jia Deng, Wei Dong, Richard Socher, Li-Jia Li, Kai Li, and Li Fei-Fei. Imagenet: A large-scale hierarchical image database. In *2009 IEEE Conference on Computer Vision and Pattern Recognition*, pages 248–255, 2009.

- [36] resnet18 x2014; Torchvision main documentation — pytorch.org. <https://pytorch.org/vision/main/models/generated/torchvision.models.resnet18.html>. [Accessed 14-03-2025].
- [37] Mark Sandler, Andrew Howard, Menglong Zhu, Andrey Zhmoginov, and Liang-Chieh Chen. Mobilenetv2: Inverted residuals and linear bottlenecks, 2019.
- [38] Ningning Ma, Xiangyu Zhang, Hai-Tao Zheng, and Jian Sun. Shufflenet v2: Practical guidelines for efficient cnn architecture design, 2018.
- [39] Leslie N. Smith and Nicholay Topin. Super-convergence: Very fast training of neural networks using large learning rates, 2018.
- [40] GitHub - weiaicunzai/pytorch-cifar100: Practice on cifar100(ResNet, DenseNet, VGG, GoogleNet, InceptionV3, InceptionV4, Inception-ResNetv2, Xception, Resnet In Resnet, ResNext, ShuffleNet, ShuffleNetv2, MobileNet, MobileNetv2, SqueezeNet, NasNet, Residual Attention Network, SENet, WideResNet) — github.com. <https://github.com/weiaicunzai/pytorch-cifar100>. [Accessed 14-03-2025].
- [41] Ilya Loshchilov and Frank Hutter. SGDR: Stochastic gradient descent with warm restarts. In *International Conference on Learning Representations*, 2017.
- [42] GitHub - chenhang98/shuffleNet-cifar10: a pytorch implement of shuffleNet on cifar-10 — github.com. <https://github.com/chenhang98/shuffleNet-cifar10/tree/master>. [Accessed 15-05-2025].
- [43] GitHub - chenhang98/mobileNet-v2_cifar10: a pytorch implement of mobileNet v2 on cifar10 — github.com. https://github.com/chenhang98/mobileNet-v2_cifar10. [Accessed 15-05-2025].

A Technical Appendices and Supplementary Material

A.1 Empirical Validation of Equation 4

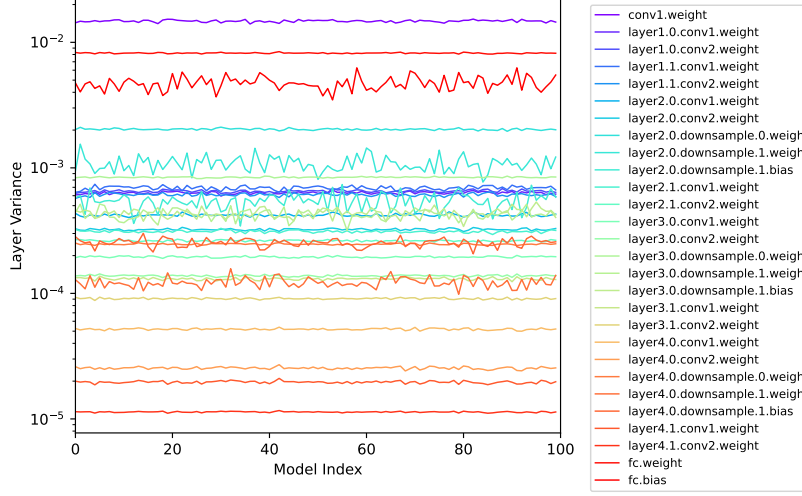


Figure 6: Layer-wise weights variance across 100 independently trained ResNet-18 models on the CIFAR-10 dataset, each initialized with a different random seed. The x-axis denotes the model index, and the y-axis represents the variance of each layer’s parameters on a logarithmic scale. Each curve corresponds to one layer, following the PyTorch naming convention. The results show that layer variances remain consistent across different runs. Batch normalization layers are excluded, as their statistics are highly sensitive to the training batches.

A.2 Empirical Validation of Equation 5

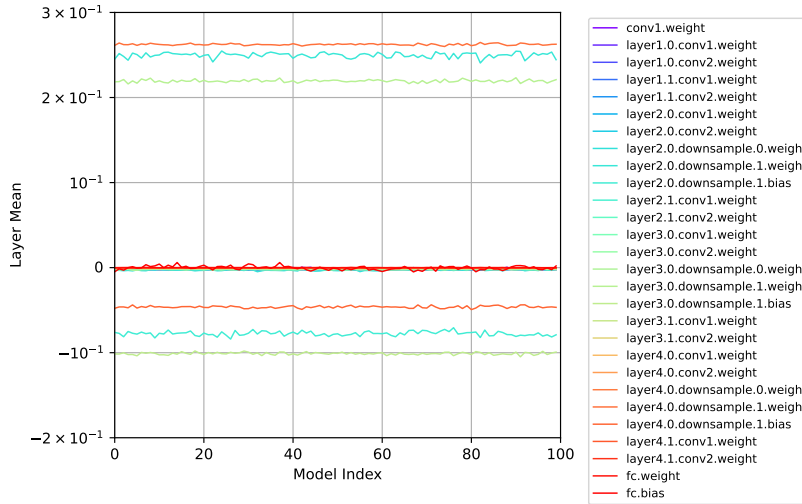


Figure 7: Layer-wise weights mean across 100 independently trained ResNet-18 models on the CIFAR-10 dataset. The figure layout follows that of Figure 6. The results indicate that the mean values of most layers are close to zero.

A.3 Proof of Equation 6

Proof of $\|\overrightarrow{OP_{l_x}}\|^2 \propto \text{Var}(\theta_{l_x})$ (approximately):

$$\text{Var}(x) = \frac{1}{n} \sum_{i=1}^n (x_i - \bar{x})^2$$

where n is the number of parameters in layer l_x , x_i denotes the i -th parameter, and \bar{x} is the mean of the parameters. Assuming Equation 5 holds, i.e., $\bar{x} \approx 0$, we have:

$$\begin{aligned} \text{Var}(x) &\approx \frac{1}{n} \sum_{i=1}^n x_i^2 \\ n \cdot \text{Var}(x) &\approx \sum_{i=1}^n x_i^2 \end{aligned}$$

By definition, the squared Euclidean distance from the origin to point P_{l_x} is:

$$\|\overrightarrow{OP_{l_x}}\|^2 = \sum_{i=1}^n x_i^2$$

Combining the two expressions, we obtain:

$$\|\overrightarrow{OP_{l_x}}\|^2 \approx n \cdot \text{Var}(x)$$

Since n is a constant for a given layer, it follows that:

$$\|\overrightarrow{OP_{l_x}}\|^2 \propto \text{Var}(\theta_{l_x})$$

which completes the proof.

A.4 Applying Algorithm 1 on additional models and datasets

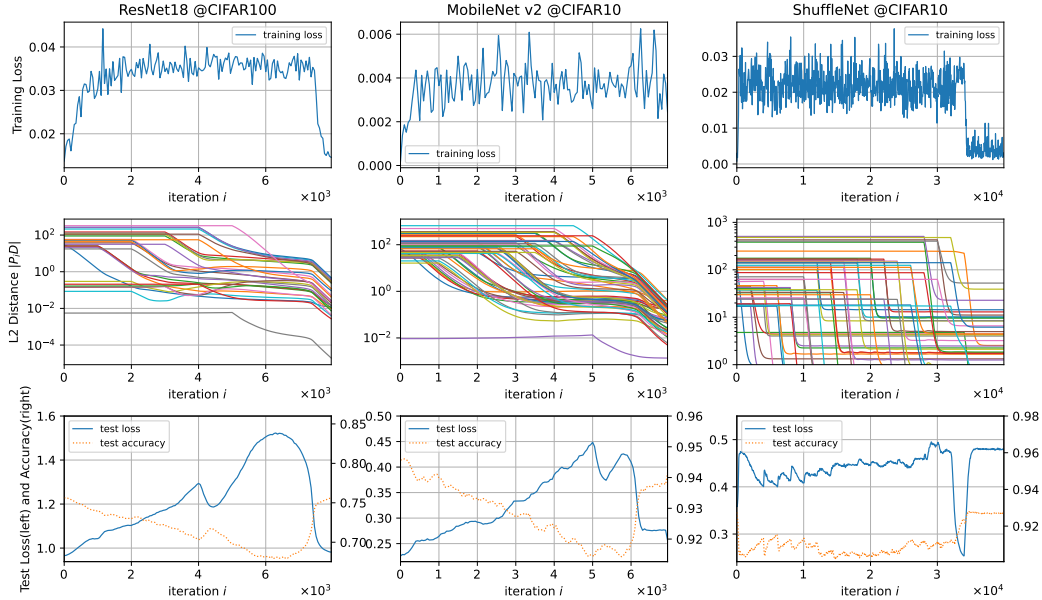


Figure 8: We apply Algorithm 1 to find the low-loss paths in LLS(ResNet18, CIFAR100), LLS(MobileNet [37], CIFAR10), LLS(ShuffleNet [38], CIFAR10). Due to computational constraints, each experiment is repeated only once. These results suggest that although different model–dataset pairs require different hyperparameters, Algorithm 1 is a generalizable method for constructing low-loss paths when properly configured.

A.5 Additional PCA results

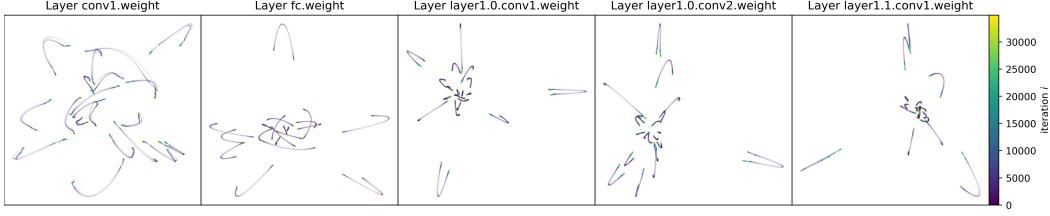


Figure 9: PCA visualization of the first five layers of LLS(ResNet18, CIFAR10). This figure is obtained by constructing low-loss paths between two sets of 20 low-loss ResNet18 models each. The first layer of ResNet18 does not show high frequency changes like LLS(LeNet5, MNIST).

A.6 Hyperparameter Table and Other Configurations

Table 1: Hyperparameters used for applying Algorithm 1 to find the low-loss path in LLS(LeNet5, MNIST), LLS(ResNet18, CIFAR10), and LLS(CCT7, CIFAR10). For ResNet18 and CCT7, the exploration is conducted in multiple phases, each involving only a subset of layers, as specified in the “Applied Layers” column. Layer names follow the PyTorch implementation of the corresponding models. Hyperparameters for Figure 8 are not listed here; please refer to the source code for details.

Applied layers		Iteration T (A1 L4 ^a)	Train round r (A1 L7)	Batch size \mathcal{B} (A1 L7)	Optimizer and hyperparameter \mathbf{x} (A1 L7)	step_a (A1 L14)	step_f (A1 L14)
LeNet5 @MNIST							
Phase 1	all	30000	5	64	SGD($\eta=0.001, \beta=0$)	0	1e-3
ResNet18 @CIFAR10							
Phase 1	all	10000	train until loss ^b <0.04 or $r>200$	256	SGD($\eta=0.001, \beta=0$)	5e-4	0
Phase 2	conv1.weight bn1.{weight+bias} fc.{weight+bias}	5000				1e-3	0
Phase 3	Phase 2 ^c layer1.* ^d	5000				1e-3	0
Phase 4	Phase 3 layer2.*	5000				1e-3	0
Phase 5	Phase 4 layer3.*	5000				1e-3	0
Phase 6	all layers	5000				1e-3	0
CCT7_3x1_32 @CIFAR10							
Phase 1	tokenizer.conv_layers classifier.{positional_emb +attention_pool +norm+fc}	5000	train until loss<0.05 or $r>10000$	128	SGD($\eta=0.001, \beta=0$)	1e-3	1e-3
Phase 2	Phase 1 classifier.blocks.0.* ^e	5000				1e-3	1e-3
Phase 3	Phase 2 classifier.blocks.1.*	5000				1e-3	1e-3
Phase 4	Phase 3 classifier.blocks.2.*	5000				1e-3	1e-3
Phase 5	Phase 4 classifier.blocks.3.*	5000				1e-3	1e-3
Phase 6	Phase 5 classifier.blocks.4.*	5000				1e-3	1e-3
Phase 7	Phase 6 classifier.blocks.5.*	5000				1e-3	1e-3
Phase 8	all layers	5000				1e-3	1e-3

^ashort for Algorithm 1 Line 4.

^bthe loss value is computed using a rolling average with a window size of 10.

^call layers in Phase 2.

^dall layers in the first bottleneck layer.

^ethe first transformer encoding block.

Table 2: Hyperparameters used for applying Algorithm 2 to find the low-loss path toward origin.

	Applied layers	Iteration T (A1 L4 ³)	Train round r (A1 L7)	Batch size \mathcal{B} (A1 L7)	Optimizer and hyperparameter \mathbf{x} (A1 L7)	step_a (A1 L14)	step_f (A1 L14)
LeNet5 @MNIST	all layers	1400	train until loss <0.02 or $r > 100$	64	SGD($\eta=0.001, \beta=0$)	1e-3	0
ResNet18 @CIFAR10	all except norm layers	1400	train until loss <0.02 or $r > 5000$	256	SGD($\eta=0.001, \beta=0$)	1e-3	0
ResNet18 @CIFAR100	all except norm layers	1400	train until loss <0.02 or $r > 5000$	256	SGD($\eta=0.001, \beta=0$)	1e-3	0
ResNet18 @ImageNet1k	all except norm layers	1000	train until loss <1.25 or $r > 50000$	128	SGD($\eta=0.001, \beta=0$)	1e-3	0
CCT7_3x1_32 @CIFAR10	all except norm layers	1000	train until loss <0.05 or $r > 5000$	128	SGD($\eta=0.001, \beta=0$)	1e-3	0

Table 3: Hyperparameters used to get a low-loss model. We use these hyperparameters to find the starting points and destination points in low-loss space.

	Training batch size	Optimizer and hyperparameters	Epoch	Learning rate η (scheduler)
LeNet5 @MNIST	64	SGD($\beta=0.9$)	20	0.01
ResNet18 @CIFAR10	256	SGD($\beta=0.9, \lambda=5e-4$)	30	OneCycle LR [39] max lr=0.1
ResNet18 @CIFAR100 [40]	256	SGD($\beta=0.9, \lambda=5e-4$)	50	OneCycle LR max lr=0.1
CCT7_3x1_32 @CIFAR10	128	AdamW($\beta_1=0.9,$ $\beta_2=0.999, \lambda=6e-2$)	300	Cosine Annealing [41] initial_lr=55e-5 warmup_lr=1e-5 min_lr=1e-5 warmup_epochs=10 cooldown_epochs=10

Table 4: Dataset preprocessing and augmentation steps. The name of each step aligns with the corresponding function names used in PyTorch. The resulting samples are used for training low-loss models and in the *Train* step in Algorithm 1 and Algorithm 2.

Data pre-processing (augmentation) steps	Step 1	Step 2	Step 3
MNIST	Random-rotate for 5 degrees	Random-crop to 28x28 with padding size 2	Normalize with dataset mean (0.1307) and standard derivation (0.3081)
CIFAR10	Random-crop to 32x32 with padding size 4	Random-horizontal-flip with probability 0.5	Normalize with mean [0.491,0.482,0.446] and standard derivation [0.247,0.243,0.262]
CIFAR100	Random-crop to 32x32 with padding size 4	Random-horizontal-flip with probability 0.5	Normalize with mean [0.507,0.487,0.441] and standard derivation [0.268,0.257,0.276]
ImageNet1k	Random-resized-crop to 224x224	Random-horizontal-flip with probability 0.5	Normalize with mean [0.485,0.456,0.406] and standard derivation [0.229,0.224,0.225]

Table 5: Computation time required to execute Algorithm 1 and Algorithm 2 on our system.

Computation time / simulation	Algorithm 1	GPU	Algorithm 2	GPU
LeNet5 @MNIST	2 hours	Nvidia RTX 3090	20 minutes	Nvidia RTX 3090
ResNet18 @CIFAR10	24 hours	Nvidia H100	10 hours	Nvidia RTX 3090
CCT7_3x1_32 @CIFAR10	48 hours	Nvidia H100	24 hours	Nvidia RTX 3090
ResNet18 @CIFAR100			4 hours	Nvidia RTX 3090
ResNet18 @ImageNet1k			340 hours	Nvidia RTX 3090

A.7 Finding Low-Loss Paths with 0.006 threshold for Resnet18@CIFAR10

In this section, we present another hyperparameter setting that could find a low-loss path within $S_{L \leq 0.006}$ ($L_{\text{thres}} = 0.006$) for ResNet18 on the CIFAR10 dataset. This threshold is lower than the minimum loss achieved by the low-loss path constructed using the AutoNEB algorithm, which reported a loss of 0.016 for ResNet20 on the CIFAR10 dataset, as shown in Table B.1 of [8]. This result demonstrates that our algorithms can identify low-loss paths with substantially lower loss values.

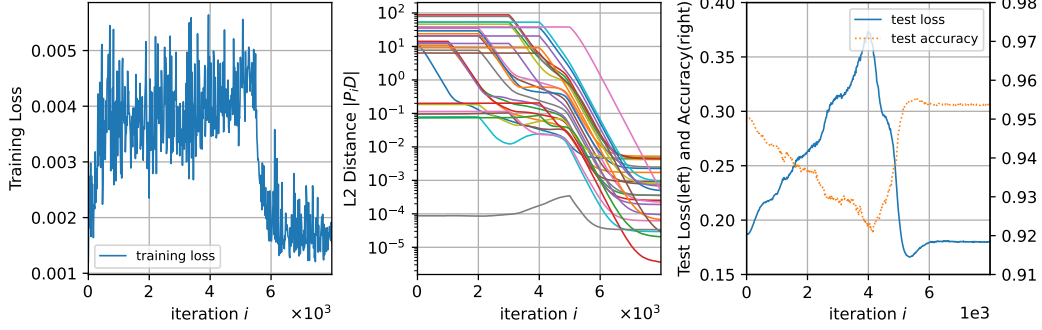


Figure 10: Training loss (left), layer-wise L2 distance (middle), and testing loss/accuracy (right) of the low-loss path constructed with a threshold of $L_{\text{thres}} = 0.006$.

Table 6: Hyperparameters used to find the low-loss path in $S_{L \leq 0.006}$.

Applied layers	Iteration T (A1 L4)	Train round r (A1 L7)	Batch size \mathcal{B} (A1 L7)	Optimizer and hyperparameter α (A1 L7)	step_a (A1 L14)	step_f (A1 L14)
ResNet18 @CIFAR10						
Phase 1 conv1.weight bn1.{weight+bias}	1000	train until loss ≤ 0.005 or $r > 20000$	128	SGD($\eta=0.001, \beta=0$)	2e-3	0
Phase 2 Phase 1 layer1.*	1000				2e-3	0
Phase 3 Phase 2 layer2.*	1000				2e-3	0
Phase 4 Phase 3 layer3.*	1000				2e-3	0
Phase 5 Phase 4 layer4.*	1000				2e-3	0
Phase 6 Phase 5 fc.{weight+bias}	3000				2e-3	0

A.8 Modification to Models

To adapt ResNet18 to the image resolution of the CIFAR dataset, the first convolutional layer is modified to use a 3×3 kernel with stride 1 and padding 1. The implementations of ShuffleNet and MobileNet for the CIFAR10 dataset are obtained from [42, 43]. For all other cases, the architecture remains identical to the original implementation.